Optics Letters

High-power thulium lasers on a silicon photonics platform

Nanxi Li,[1,2,*] Purnawirman,[1] Zhan Su,[1] E. Salih Magden,[1] Patrick T. Callahan,[1] Katia Shtyrkova,[1] Ming Xin,[1] Alfonso Ruocco,[1] Christopher Baiocco,[3] Erich P. Ippen,[1] Franz X. Kärtner,[1,4] Jonathan D. B. Bradley,[1,5] Diedrik Vermeulen,[1] and Michael R. Watts[1]

[1]Department of Electrical Engineering and Research Laboratory of Electronics, Massachusetts Institute of Technology, 77 Massachusetts Avenue, Cambridge, Massachusetts 02139, USA
[2]John A. Paulson School of Engineering and Applied Sciences, Harvard University, 29 Oxford Street, Cambridge, Massachusetts 02138, USA
[3]College of Nanoscale Science and Engineering, State University of New York, 257 Fuller Road, Albany, New York 12203, USA
[4]Center for Free-Electron Laser Science, DESY and Hamburg University, Notkestraße 85, 22607 Hamburg, Germany
[5]Currently at Department of Engineering Physics, McMaster University, 1280 Main Street West, Hamilton, Ontario L8S 4L7, Canada
*Corresponding author: nanxili@mit.edu

Received 21 November 2016; accepted 16 February 2017; posted 27 February 2017 (Doc. ID 281198); published 15 March 2017

Mid-infrared laser sources are of great interest for various applications, including light detection and ranging, spectroscopy, communication, trace-gas detection, and medical sensing. Silicon photonics is a promising platform that enables these applications to be integrated on a single chip with low cost and compact size. Silicon-based high-power lasers have been demonstrated at 1.55 μm wavelength, while in the 2 μm region, to the best of our knowledge, high-power, high-efficiency, and monolithic light sources have been minimally investigated. In this Letter, we report on high-power CMOS-compatible thulium-doped distributed feedback and distributed Bragg reflector lasers with single-mode output powers up to 267 and 387 mW, and slope efficiencies of 14% and 23%, respectively. More than 70 dB side-mode suppression ratio is achieved for both lasers. This work extends the applicability of silicon photonic microsystems in the 2 μm region.

OCIS codes: (130.3120) Integrated optics devices; (140.0140) Lasers and laser optics; (230.5750) Resonators.

https://doi.org/10.1364/OL.42.001181

Laser sources in the 2 μm wavelength region have many applications, such as light detection and ranging, spectroscopy, optical waveform generation and synthesis, material processing, communication, and trace-gas detection systems. The high water absorption at 2 μm also makes such lasers good candidates for medical applications [1]. Furthermore, 2 μm wavelength lasers in pulsed mode could be used as pumps for nonlinear processes in silicon, such as mid-IR optical parametric amplification [2]. Silicon is the material of choice for both microelectronic circuits and integrated photonics components around 1.31 and 1.55 μm. To extend the applicability of silicon photonics microsystems to the 2 μm wavelength region, complementary metal-oxide semiconductor (CMOS)-compatible integrated laser sources around 2 μm are critical. These lasers will enable highly compact devices that can perform the task of current complex bulky laboratory setups.

Among the methods to integrate lasers on a silicon platform [3–6], deposition of rare-earth-doped Al_2O_3 glass has proven to be effective due to several advantages. First, rare-earth-doped Al_2O_3 glass can be deposited as a single-step back-end-of-line process on silicon wafers without requiring any additional etch steps [7–10]. Second, common rare-earth materials such as erbium and thulium have a wide emission spectrum, which enables wavelength tunability and design flexibility [11–13]. Third, the rare-earth-doped gain media do not involve free carriers as semiconductor lasers do, enabling low losses and lasers with narrow linewidths [14–16]. Lastly, the low thermo-optic effect of the host medium enables operation over a wide temperature range [17]. The state-of-the-art for high-power lasers fabricated using this methodology was demonstrated to be 75 mW continuous-wave output power in an erbium-doped waveguide laser operating around 1.55 μm [18]. Among rare-earth elements, thulium is particularly attractive for integrated lasers on silicon since its emission spectrum is around 2 μm. Integrated thulium-doped channel waveguide lasers on tungstate were reported with high power and slope efficiencies [19,20]. However, so far work on thulium-doped high-power lasers on a CMOS-compatible platform has been absent.

Prior to this work, we have reported a thulium-doped microcavity laser with sub-milliwatt output power and multi-mode operation [21,22]. However, high output power and single-mode operation are desired for many applications. In this Letter, we demonstrate high-power thulium-doped waveguide lasers that were fabricated on silicon chips in a 300 mm CMOS foundry. An Al_2O_3:Tm^{3+} thin film deposited as a gain medium on top of a buried Si_3N_4 strip in SiO_2 acts as a rib waveguide on a silicon substrate. The narrow reflection bandwidths of distributed feedback (DFB) and distributed

Bragg reflector (DBR) structures enable single-mode output. The maximum on-chip lasing powers achieved for the DFB and DBR devices were 267 and 387 mW, with slope efficiencies of 14% and 23%, respectively.

The waveguide cross section of the DFB laser is shown in Fig. 1(a). The width and separation of the Si_3N_4 bars are optimized to be 300 and 350 nm, respectively, to provide high mode confinements for both pump and signal modes within the Al_2O_3:Tm^{3+} film. The confinement factors within the thulium-doped gain region for pump and signal are calculated to be 90% and 85%, respectively, using a finite-difference 2D mode solver. The oxide gap between the Si_3N_4 layer and the Al_2O_3 layer is 200 nm. The refractive indices of the materials used in our laser at both pump and signal wavelengths are listed in Fig. 1(b). The transverse-electric (TE) field intensity of the fundamental mode is shown in Fig. 1(c). For the DBR laser, the gain waveguide cross section has seven Si_3N_4 bars instead of five. Gratings are added on both sides of the gain waveguide. We designed DFB and DBR cavities for different laser wavelengths by varying the grating periods.

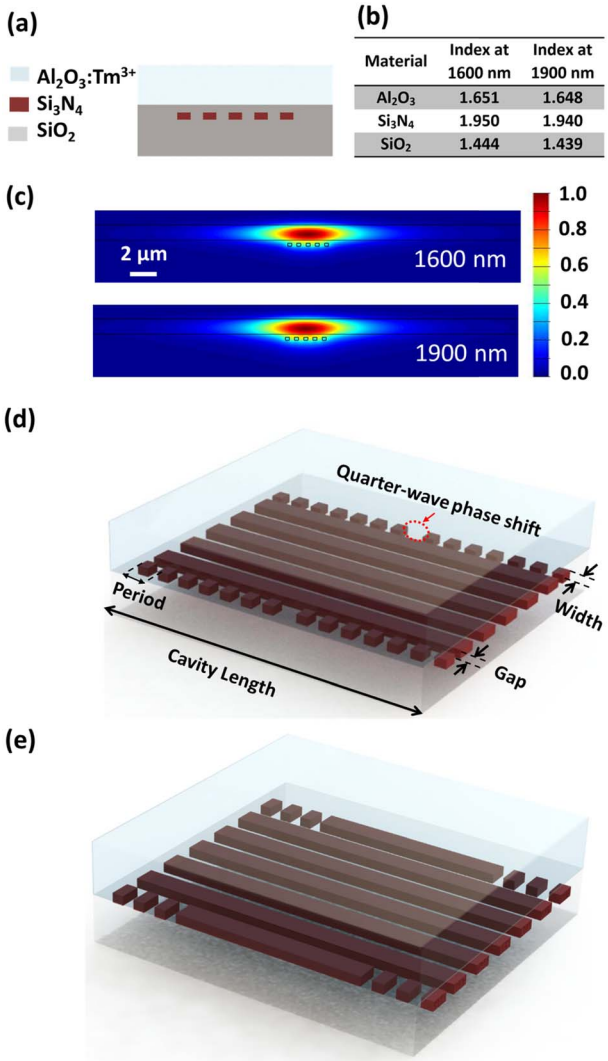

Fig. 1. Integrated thulium DFB and DBR laser designs. (a) Cross section of the laser gain waveguide including five strips of Si_3N_4. (b) Refractive indices of the waveguide materials at both pump and signal wavelengths. (c) Fundamental TE field intensity for the pump (1600 nm) and laser output (1900 nm) wavelengths in the DFB waveguide. 3D illustrations of (d) the DFB laser and (e) the DBR laser, showing the different material layers and cavity features (not to scale).

Perspective views of the DFB and DBR lasers are illustrated in Figs. 1(d) and 1(e), respectively. For the DFB laser, the lateral gap between the grating and gain waveguide is designed to be 450 nm, and the grating width is chosen to be 260 nm in order to provide enough feedback at the designed laser wavelength. The coupling coefficient (κ) is calculated to be 1.0×10^3 m^{-1}. For the DBR laser, the grating width and gap follow the pattern of seven Si_3N_4 strips of gain waveguide between two DBR mirrors, with coupling coefficient (κ) of 1.3×10^3 m^{-1}. The cavity lengths for both lasers are 2 cm, limited by the maximum length of the chip. For a laser cavity length shorter than 2 cm, with the same pump power, the lasing power decreases. The coupling coefficient and cavity length product ($\kappa \cdot L$) for DFB and DBR are 20 and 26, respectively. By characterizing the cavity response of the DBR laser, the reflectivity of the grating on each side is estimated to be 70%. Such grating reflectivity enables the laser to achieve a few hundred milliwatts of output power, while still maintaining relatively high Q of the DBR cavity. The effective refractive index (n_{eff}) of the waveguide is calculated using a finite-difference 2D mode solver, considering the grating as perturbations on both sides of the segmented Si_3N_4-rib to provide feedback. The n_{eff} is calculated to be 1.565. The grating period (Λ) can be obtained using the following equation:

$$\Lambda = \frac{\lambda}{2n_{\text{eff}}}, \tag{1}$$

where λ is the designed laser wavelength.

The lasers were fabricated in a state-of-the-art CMOS foundry on a 300 mm silicon wafer. The fabrication process is illustrated in Fig. 2(a). The Si_3N_4 layer is deposited on top of a SiO_2 layer, both via plasma-enhanced chemical-vapor deposition (PECVD), followed by a surface polishing process to reduce optical scattering loss. Then the Si_3N_4 layer is patterned using 193 nm immersion lithography and reactive ion etching, as shown in step II. Next, in step III, we deposit a SiO_2 layer and planarize the top surface via chemical-mechanical polishing. The thickness of the SiO_2 layer on the Si_3N_4 layer is 200 nm. After that, the Al_2O_3:Tm^{3+} film is deposited at a thickness of 1100 nm via reactive co-sputtering, as shown in step IV. The substrate temperature is measured to be 350°C using a thermocouple directly in contact with chip. The background loss of the Al_2O_3:Tm^{3+} film is measured to be <0.1 dB/cm. Fabrication runs with different doping levels revealed an optimum Tm^{3+} doping concentration of 3.0×10^{20} cm^{-3}. At the same pump power, but lower doping concentration, the lasing power of the device decreases due to lower gain; while for higher doping concentration, the lasing power of the device decreases due to doped-ion clustering or quenching [18,23,24]. In order to visualize the Si_3N_4 pattern, after step III and before step IV, 140s hydrogen fluoride (HF) etching is used to remove the SiO_2 top cladding. A scanning electron microscope (SEM) image of the gain waveguide and side gratings is shown in Fig. 2(b).

The measurement setup for characterizing the lasers is illustrated in Fig. 3(a). A laser source at 1612 nm together with an L-band erbium-doped fiber amplifier (EDFA) were used for optical pumping. A polarization controller was used to ensure

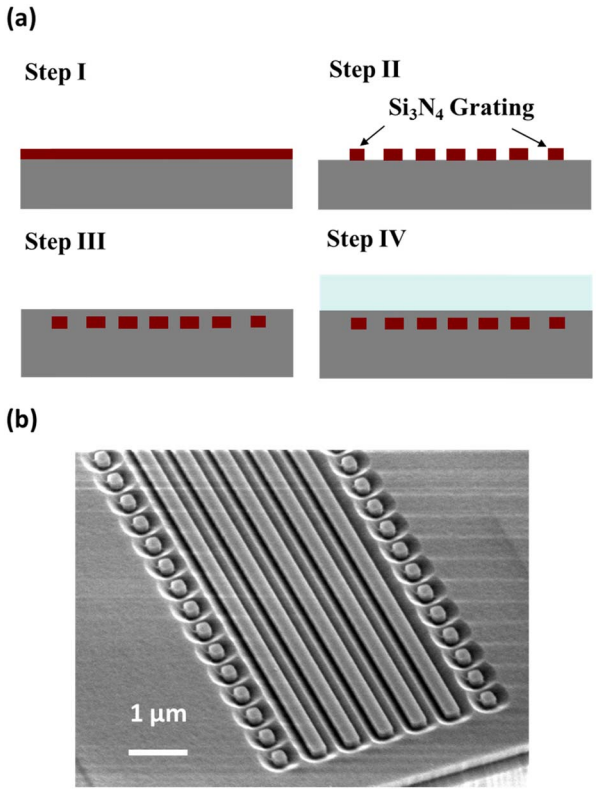

Fig. 2. (a) Laser fabrication steps: (I) deposition of Si_3N_4 layer via PECVD; (II) pattering of Si_3N_4 layer yielding five-segment (DFB) or seven-segment (DBR) waveguides in the center for mode confinement and additional periodic segments at each side for distributed feedback; (III) deposition of SiO_2 followed by top surface planarization; (IV) deposition of the thulium-doped Al_2O_3 gain medium by reactive co-sputtering. (b) SEM image of the Si_3N_4 pattern after HF etching of the SiO_2 top cladding from Step III.

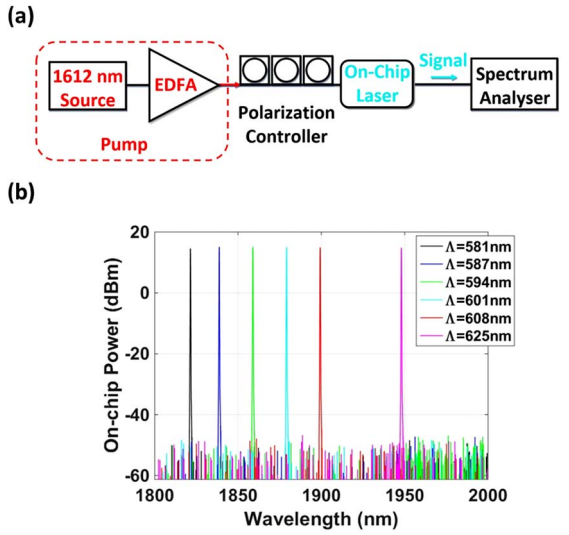

Fig. 3. (a) Measurement setup: a 1612 nm laser source together with a high-power EDFA, followed by a polarization controller to ensure that the fundamental TE mode is coupled into the gain waveguide of the laser. An optical spectrum analyzer is used to capture the spectrum; (b) output spectrum of DFB lasers with different grating periods, showing single-mode lasing at 1820, 1840, 1860, 1880, 1900, and 1950 nm.

that the pump light was coupled into the fundamental TE mode of the gain waveguide. A cleaved single-mode SMF-28 fiber was used to butt-couple the pump light onto the chip, and another cleaved single-mode SM-2000 fiber was used to butt-couple the output signal of the laser from the chip. The fiber-to-chip coupling losses were measured to be 7.1 dB for SMF-28 at the pump wavelength, and 7.9 dB for SM-2000 at the laser output wavelength. The output signal was coupled into an optical spectrum analyzer (Yokogawa AQ6375) to capture the spectrum. The grating period design variations are 581, 587, 594, 601, 608, and 625 nm. They were calculated using Eq. (1), with corresponding wavelengths at 1820, 1840, 1860, 1880, 1900, and 1950 nm, respectively. The measured optical spectra of the corresponding DFB laser designs are shown in Fig. 3(b). Within the broad gain bandwidth of the Al_2O_3:Tm^{3+}, we are able to precisely control the laser wavelength by choosing the proper grating period.

From the DFB and DBR laser grating period design variations, we selected the devices that operate near the peak of the thulium emission spectrum for the lasing slope efficiency measurements. The slope efficiency curves for DFB and DBR lasers are shown in Figs. 4(a) and 4(b), respectively. The maximum on-chip laser output power of the DFB and DBR lasers were measured to be 267 and 387 mW, respectively. The powers were measured from a single output end of the lasers, and the fiber coupling losses are calibrated out. An equivalent level of power could be obtained when pump is launched from the other side of the laser, considering the symmetry of the cavity. Using linear curve fitting, the single-sided slope efficiencies for the DFB and DBR lasers were found to be 14% and 23%, with

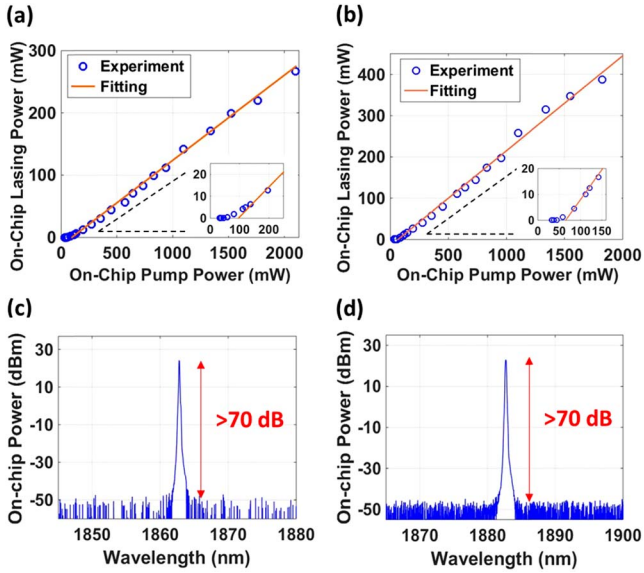

Fig. 4. (a) DFB and (b) DBR laser output curves, showing 14% and 23% slope efficiency, 267 and 387 mW maximum output power, and 96 and 65 mW lasing threshold, respectively. The output spectra of (c) DFB and (d) DBR lasers at 1861 nm and 1881 nm, respectively, obtained with up to 2 W on-chip pump power and showing side-mode suppression ratios >70 dB.

laser thresholds of 96 and 65 mW at 1612 nm pumping. The peak laser wavelengths with up to 2 W on-chip pump power for the DFB and DBR lasers were recorded by the spectrum analyzer, as shown in Figs. 4(c) and 4(d), respectively. Single-mode operation was enabled by the narrow bandwidth grating. The side-mode suppression ratio reached more than 70 dB.

In summary, we have designed, fabricated, and characterized high-power thulium DFB and DBR lasers integrated on a silicon chip. A CMOS-compatible segmented Si_3N_4 rib waveguide was used to form the laser cavity. Gratings were added on both sides of the segmented Si_3N_4 rib waveguide to provide feedback and thulium-doped Al_2O_3 glass was used as the gain medium. By varying the grating period, single-mode lasers with wavelengths from 1800 to 1950 nm have been demonstrated within the thulium gain bandwidth. The highest DFB and DBR output powers of 267 and 387 mW under 1612 nm pumping were measured at 1861 nm and 1881 nm wavelengths, with slope efficiencies of 14% and 23%, respectively. More than 70 dB side-mode suppression, which enables high signal-to-noise ratio for chip-scale communication and spectroscopic applications, was observed.

Funding. Defense Advanced Research Projects Agency (DARPA) (HR0011-15-C-0056).

Acknowledgment. The authors would like to acknowledge Professor Federico Capasso for helpful discussion, Gary Riggott and Kurt Broderick for assistance on thulium-doped thin film deposition, and Di Zhu for assistance with SEM imaging. N. Li is sponsored by National Science Scholarship (NSS) from the Agency of Science, Technology and Research (A*STAR), Singapore. K. Shtyrkova is sponsored by National Defense Science and Engineering Graduate Fellowship (32 CFR 168a).

REFERENCES

1. S. L. K. Scholle, P. Koopmann, and P. Fuhrberg, in *Proceedings of Frontiers in Guided Wave Optics and Optoelectronics* (2010), pp. 471–500.
2. X. Liu, R. M. Osgood, Y. A. Vlasov, and M. J. GreenWilliam, Nat. Photonics **4**, 557 (2010).
3. A. W. Fang, E. Lively, Y.-H. Kuo, D. Liang, and J. E. Bowers, Opt. Express **16**, 4413 (2008).
4. H. Rong, R. Jones, A. Liu, O. Cohen, D. Hak, A. Fang, and M. Paniccia, Nature **433**, 725 (2005).
5. J. Liu, X. Sun, R. Camacho-Aguilera, L. C. Kimerling, and J. Michel, Opt. Lett. **35**, 679 (2010).
6. G. Singh, Purnawirman, J. D. B. Bradley, N. Li, E. S. Magden, M. Moresco, T. N. Adam, G. Leake, D. Coolbaugh, and M. R. Watts, Opt. Lett. **41**, 1189 (2016).
7. K. Wörhoff, J. D. B. Bradley, F. Ay, D. Geskus, T. P. Blauwendraat, and M. Pollnau, IEEE J. Quantum Electron. **45**, 454 (2009).
8. E. S. Magden, Purnawirman, N. Li, G. Singh, J. D. B. Bradley, G. S. Petrich, G. Leake, D. D. Coolbaugh, M. R. Watts, and L. A. Kolodziejski, in *Conference on Lasers and Electro-Optics (CLEO)* (2016), paper SM1G.2.
9. M. Belt and D. J. Blumenthal, Opt. Express **22**, 10655 (2014).
10. Z. Su, J. D. B. Bradley, N. Li, E. S. Magden, P. Purnawirman, D. Coleman, N. Fahrenkopf, C. Baiocco, T. N. Adam, G. Leake, D. Coolbaugh, D. Vermeulen, and M. R. Watts, in *Advanced Photonics (IPR, NOMA, Sensors, Networks, SPPCom, SOF)* (2016), paper IW1A.3.
11. S. Li, D. Zhang, J. Zhao, Q. Yang, X. Xiao, S. Hu, L. Wang, M. Li, X. Tang, Y. Qiu, M. Luo, and S. Yu, Opt. Express **24**, 6341 (2016).
12. N. Li, E. Timurdogan, C. V. Poulton, M. Byrd, E. S. Magden, Z. Su, Purnawirman, G. Leake, D. D. Coolbaugh, D. Vermeulen, and M. R. Watts, Opt. Express **24**, 22741 (2016).
13. Y. Liu, K. Wu, N. Li, L. Lan, S. Yoo, X. Wu, P. P. Shum, S. Zeng, and X. Tan, J. Opt. Soc. Korea **17**, 357 (2013).
14. Y. W. Song, S. A. Havstad, D. Starodubov, Y. Xie, A. E. Willner, and J. Feinberg, IEEE Photon. Technol. Lett. **13**, 1167 (2001).
15. E. H. Bernhardi, H. A. G. M. van Wolferen, L. Agazzi, M. R. H. Khan, C. G. H. Roeloffzen, K. Wörhoff, M. Pollnau, and R. M. de Ridder, Opt. Lett. **35**, 2394 (2010).
16. M. Belt, T. Huffman, M. L. Davenport, W. Li, J. S. Barton, and D. J. Blumenthal, Opt. Lett. **38**, 4825 (2013).
17. M. Belt and D. J. Blumenthal, in *Optical Fiber Communications Conference and Exhibition (OFC)* (2015), pp. 1–3.
18. E. S. Hosseini, Purnawirman, J. D. B. Bradley, J. Sun, G. Leake, T. N. Adam, D. D. Coolbaugh, and M. R. Watts, Opt. Lett. **39**, 3106 (2014).
19. K. van Dalfsen, S. Aravazhi, C. Grivas, S. M. García-Blanco, and M. Pollnau, Opt. Lett. **37**, 887 (2012).
20. K. van Dalfsen, S. Aravazhi, C. Grivas, S. M. García-Blanco, and M. Pollnau, Opt. Lett. **39**, 4380 (2014).
21. Z. Su, N. Li, E. Salih Magden, M. Byrd, Purnawirman, T. N. Adam, G. Leake, D. Coolbaugh, J. D. B. Bradley, and M. R. Watts, Opt. Lett. **41**, 5708 (2016).
22. J. D. B. Bradley, Z. Su, E. S. Magden, N. Li, M. Byrd, Purnawirman, T. N. Adam, G. Leake, D. Coolbaugh, and M. R. Watts, Proc. SPIE **9744**, 97440U (2016).
23. N. Li, Purnawirman, J. D. B. Bradley, G. Singh, E. S. Magden, J. Sun, and M. R. Watts, in *Optoelectronics Global Conference (OGC)* (2015), pp. 1–2
24. L. Agazzi, K. Wörhoff, and M. Pollnau, J. Phys. Chem. C **117**, 6759 (2013).